



HAL
open science

Switchbacks in the Young Solar Wind: Electron Evolution Observed inside Switchbacks between 0.125 au and 0.25 au

Raaman Nair, Jasper Halekas, Phyllis Whittlesey, Davin Larson, Roberto Livi, Matthieu Berthomier, Justin Kasper, Anthony Case, Michael Stevens, Stuart Bale, et al.

► To cite this version:

Raaman Nair, Jasper Halekas, Phyllis Whittlesey, Davin Larson, Roberto Livi, et al.. Switchbacks in the Young Solar Wind: Electron Evolution Observed inside Switchbacks between 0.125 au and 0.25 au. *The Astrophysical Journal*, 2022, 936 (2), pp.164. 10.3847/1538-4357/ac88c4 . hal-04306023

HAL Id: hal-04306023

<https://hal.science/hal-04306023>

Submitted on 27 Nov 2023

HAL is a multi-disciplinary open access archive for the deposit and dissemination of scientific research documents, whether they are published or not. The documents may come from teaching and research institutions in France or abroad, or from public or private research centers.

L'archive ouverte pluridisciplinaire **HAL**, est destinée au dépôt et à la diffusion de documents scientifiques de niveau recherche, publiés ou non, émanant des établissements d'enseignement et de recherche français ou étrangers, des laboratoires publics ou privés.



Switchbacks in the Young Solar Wind: Electron Evolution Observed inside Switchbacks between 0.125 au and 0.25 au

Raaman Nair¹ , Jasper S. Halekas¹ , Phyllis L. Whittlesey² , Davin E. Larson² , Roberto Livi² , Matthieu Berthomier³, Justin C. Kasper^{4,5} , Anthony W. Case⁶ , Michael L. Stevens⁵ , Stuart D. Bale² , Robert J. MacDowall⁷ , and Marc P. Pulupa²

¹ Department of Physics and Astronomy, University of Iowa, Iowa City, IA, USA; raaman-nair@uiowa.edu

² Space Sciences Laboratory, University of California, Berkeley, CA, USA

³ Laboratoire de Physique des Plasmas, CNRS, Sorbonne Université, Ecole Polytechnique, Observatoire de Paris, Université Paris-Saclay, Paris, France

⁴ Climate and Space Sciences and Engineering, University of Michigan, Ann Arbor, MI, USA

⁵ Smithsonian Astrophysical Observatory, Cambridge, MA, USA

⁶ Harvard-Smithsonian Center for Astrophysics, Cambridge, MA, USA

⁷ Laboratory for Extraterrestrial Physics, NASA Goddard Space Flight Center, Greenbelt, MD, USA

Received 2022 June 20; revised 2022 August 6; accepted 2022 August 9; published 2022 September 12

Abstract

Switchbacks are localized deviations from the nominal Parker spiral field in the solar wind. In this study, we investigate the electron distributions inside switchbacks, focusing primarily on the suprathermal (halo and strahl) populations. We explore electron parameters in relation to the angle of rotation of the magnetic field from radial to determine whether electron distributions observed within switchbacks have any differences from those outside of switchbacks. Our observations reveal several trends in the suprathermal electron populations inside switchbacks. We find that the sunward deficit in the electron velocity distribution function typically observed near the Sun is filled in at larger rotation angles. This results in the suprathermal electron density and heat flux in the antistrahl direction changing from a negative to a positive value. On many days, we also observe a positive correlation between the halo density and rotation angle, and this may suggest that the growth of the halo may fill in the sunward deficit. We also find that strahl distributions have an increased average angular spread at large magnetic field rotation angles. The increase in suprathermal electron flux in the antistrahl direction, and the increase in strahl width, together could suggest that enhanced scattering occurs inside switchbacks. Electron core beta values tend to increase with the magnetic field rotation angle, mainly due to a decrease in magnetic pressure. An increase in electron beta may favor the growth of instabilities inside switchbacks. The Parker Solar Probe observations therefore support an enhanced role for wave–particle interactions in switchbacks.

Unified Astronomy Thesaurus concepts: Solar wind (1534); Space plasmas (1544); Solar corona (1483); Solar magnetic fields (1503); Solar physics (1476)

1. Introduction

Switchbacks are discrete rotations of the interplanetary magnetic field (Yamauchi et al. 2004; Landi et al. 2006; Matteini et al. 2014; Borovsky 2016; Tenerani et al. 2020; Mozer et al. 2021). Switchbacks are known to exhibit a continuous spectrum of deviations from the nominal Parker spiral field direction (Dudok de Wit et al. 2020). At some times, these rotations are large enough that they can exhibit a sign change in the radial component of the magnetic field; thus the term *switchback* (McManus et al. 2019; Krasnoselskikh et al. 2020; Squire et al. 2020; Woolley et al. 2020; Mozer et al. 2021). Switchbacks in the solar wind are not a new discovery. Several spacecraft prior to the Parker Solar Probe (PSP) have detected switchbacks, including the Ulysses (Balogh et al. 1999; Larosa et al. 2021) and Helios (Borovsky 2016; Horbury et al. 2018; Larosa et al. 2021) space missions. In recent years, ESA’s Solar Orbiter has also observed switchbacks in the solar wind (Fedorov et al. 2021). What is unique about PSPs in situ observations is how ubiquitous the switchback features are in the environment near the Sun (Dudok de Wit et al. 2020;

Larosa et al. 2021). This observation may indicate that switchbacks are structures formed near the Sun (Yamauchi et al. 2004; Tenerani et al. 2020), though this remains uncertain. Switchbacks can vary in duration and amplitude (Horbury et al. 2018; Dudok de Wit et al. 2020; Mozer et al. 2020) and have been observed at various distances from the Sun (Balogh et al. 1999; Horbury et al. 2018; Tenerani et al. 2020). The nature of switchbacks also remains to be investigated. Several studies have stated that switchbacks are purely Alfvénic features (Squire et al. 2020; Woolley et al. 2020; Shoda et al. 2021), while others suggest that switchbacks are not purely Alfvénic structures but rather mixtures of both Alfvénic and magnetosonic-like properties (Zank et al. 2020; Larosa et al. 2021). As PSP gets ever closer to the Sun, it reveals more and more about the nature of switchbacks.

In the solar wind, various scattering mechanisms are in play to alter the electron velocity distribution function (eVDF) (Cuperman et al. 1972; Hollweg 1974; Vocks & Mann 2009; Bale et al. 2013; Boldyrev & Horaites 2019; Horaites et al. 2019; Halekas et al. 2020; Micera et al. 2020; Berčič et al. 2021; Cattell et al. 2021). These include, but are not limited to, Coulomb collisions (Scudder & Olbert 1979a, 1979b; Salem et al. 2003; Landi et al. 2012; Boldyrev & Horaites 2019), electrostatic modes (Gary 1978; Roberg-Clark et al. 2018; López et al. 2020), quasi-parallel whistler-mode waves (Gary

et al. 1975, 1994, 1999; Saeed et al. 2017; Shaaban et al. 2018), oblique whistler waves/magnetosonic instabilities (Horaites et al. 2018; Vasko et al. 2019; Verscharen et al. 2019; Micera et al. 2020), and firehose instability (Innocenti et al. 2020).

The eVDF of the solar wind typically consists of three components: core electron, halo electron, and strahl electron population (Štverák et al. 2009; Feldman et al. 1975; Rosenbauer et al. 1977; Pilipp et al. 1987; Maksimovic et al. 2005). The core can be modeled by a bi-Maxwellian distribution fit and makes up most of the electron population in the solar wind. At higher velocities, deviations from the Maxwellian start to appear as tails, and these are the suprathermal electrons (strahl and halo). The strahl generally moves away from the Sun along the magnetic field. To distinguish switchbacks from current sheets, we look at the polarity of the strahl population, which is aligned with the magnetic field, and always travels outward from the Sun (Meng et al. 2022). When PSP crosses the heliospheric current sheet (HCS), the polarity of the strahl population is also reversed, whereas the polarity of the strahl remains constant when crossing a switchback. Typically, the strahl appears as an extended shoulder above the core fit on the anti-sunward direction in an eVDF. The halo population displays a much more dispersed pitch angle distribution and is commonly fitted by a bi-Kappa function (Štverák et al. 2009; Maksimovic et al. 1997, 2005). Prevailing theories suggest that the halo may be a by-product of a multiple scattering process that disperses beam-like strahl to a more isotropic population (Saito & Peter Gary 2007; Kajdic et al. 2016; Graham et al. 2017; Horaites et al. 2018; Berčič et al. 2019; Verscharen et al. 2019; Halekas et al. 2021).

Recent observations from PSP close to the Sun have also revealed a deficit in the sunward suprathermal electron population (Kasper et al. 2016; Halekas et al. 2020; Berčič et al. 2020; Whittlesey et al. 2020; Halekas et al. 2021), where the electron distribution falls below a Maxwellian. Halekas et al. 2021 showed that the occurrence of these deficits was anticorrelated with the presence of halo electrons in the solar wind. These observations motivate us to investigate whether a similar trend occurs inside switchbacks. Additionally, while several papers have discussed ions inside switchbacks (Mozer et al. 2020; Woolley et al. 2020; Woodham et al. 2021), electrons inside switchbacks remain to be investigated. This study investigates the electron content inside switchbacks to better understand how the solar wind evolves close to the Sun.

2. Method

Utilizing measurements from the Solar Wind Electrons, Alphas, and Protons (SWEAP)/SPAN-Electron (SPAN-E) (Whittlesey et al. 2020) suite on the PSP (SPAN Ae and SPAN B), we analyze electron distributions inside switchbacks at heliocentric distances of 0.125–0.25 au. The SWEAP package consists of three electrostatic analyzers (SPANs). Two of the three SPAN sensors are dedicated to electron detection; SPAN Ae and SPAN B. SPAN Ae face *forward* (ram side), and SPAN B looks *behind* the spacecraft (anti-ram side). Together, the two electron sensors capture about 90% of the sky. The heat shield and other spacecraft obstructions block most of the remaining field of view (FOV). The sensors can also measure 3D electron velocity distribution functions (eVDFs) in the inner heliosphere. We utilized Level 2 (electron distributions) data from SPAN Ae and B to perform our

statistical analysis. The FIELDS data set (Bale et al. 2016) was also used to obtain the magnetic field, which is used to organize the electron distributions. The cadence of each sample measurement during the periods utilized in this paper is 11–13 s. Further details of the PSP instruments are described in other sources (Fox et al. 2016; Bale et al. 2016; Kasper et al. 2016; Case et al. 2020; Whittlesey et al. 2020).

We use the heliocentric RTN coordinate system to organize our observations. The radial (R) component points from the Sun center to the spacecraft. The tangential (T) component points toward the Sun’s prograde rotation, and the normal (N) component completes the right-handed triad. We also utilized magnetic field-aligned (FA) coordinates to organize the electron distributions. The electron pitch angle (α) is defined as the angle between the local magnetic field vector (B field) and the electron velocity vector. A pitch angle of 0° corresponds to an electron moving parallel to the B field and 180° antiparallel to the B field.

Due to the high Alfvénicity of switchbacks (Kasper et al. 2019; Bale et al. 2019; Woolley et al. 2020; Larosa et al. 2021), changes in the total magnetic field during a switchback period are typically small. Hence, our focus will be on the radial component of the magnetic field. To distinguish a switchback feature from the local Parker spiral, we must consider the radial distance, latitude, and the background solar wind speed during the time of the measurement (Chang et al. 2019). To estimate the geometry of the Parker spiral at a given location, we use the Parker solution (Parker 1958),

$$\tan \phi_r = \frac{\Omega_\odot \sin \theta}{u_{sw}} (R_\odot - r). \quad (1)$$

Here, r is the radial distance of PSP from the Sun (au), $R_\odot = 0.005$ au is the radius of the Sun, u_{sw} is the measured solar wind speed (km s^{-1}), $\Omega_\odot = 2.7 \times 10^{-6}$ rad s^{-1} , is the angular velocity of the Sun, θ is the latitude of the solar wind from the Sun’s equator, and ϕ_r is the azimuthal Parker spiral angle at radial distance, r . The solar wind speed is obtained from the Solar Probe Cup (SPC; Case et al. 2020). PSP’s orbit is in the ecliptic plane (Whittlesey et al. 2020; Guo et al. 2021); thus, there is no $\sin(\theta)$ component. This simplifies Equation (1) to the following form:

$$\phi_r = \tan^{-1} \left[\frac{\Omega_\odot}{u_{sw}} (R_\odot - r) \right]. \quad (2)$$

Depending on PSP’s position and the solar activity, the average proton wind speed ranges from about 220–415 km s^{-1} , and the Parker spiral angle ranges from around 9° – 22° . Figure 3 shows the nominal Parker spiral angle for 2018 November 2 (as estimated from Equation (2) and ignoring the negative sign for directionality) overlaid on the magnetic field rotation. For comparison, the Parker spiral angle around Mercury is about 30° (Korth et al. 2011), approximately 45° near-Earth (Svalgaard & Wilcox 1974), and close to 90° beyond 10 au (Meyer-Vernet 2007).

Our study focused on 42 days of PSP observations (at or close to perihelion) over six PSP encounters. Table 1 summarizes the electron parameters we observed on these six encounters. For each day of observations, we note electron parameter trends with magnetic field rotation angle/B angle (ψ) as either negative correlation with rotation angle, inconclusive,

Table 1
Observed Electron Parameters with Respect to Magnetic Field Rotation for Six Encounters (42 Days Total)

	[Negative Correlation: Inconclusive: Positive Correlation]					
Parameter	Encounter 1 (11 days)	Encounter 2 (10 days)	Encounter 3 (3 days)	Encounter 4 (6 days)	Encounter 5 (7 days)	Encounter 6 (5 days)
Core n	0:7:4	0:8:2	0:2:1	0:3:3	0:4:3	0:2:3
Core Tpar	1:10:0	2:8:0	0:3:0	2:4:0	3:4:0	2:2:1
Halo n	0:3:8	0:5:5	0:1:2	0:1:5	0:1:6	0:4:1
Strahl n	1:10:0	3:6:1	0:3:0	1:5:0	0:6:1	1:3:1
Antistrahl direction Suprathermal n (Core deficit)	0:3:8	0:1:9	0:0:3	0:1:5	0:0:7	1:1:3
Strahl direction Suprathermal n	2:9:0	0:9:1	0:3:0	0:6:0	1:3:3	2:3:0
Antistrahl direction Suprathermal q	0:1:10	0:3:7	0:0:3	0:0:6	0:1:6	0:3:2
Strahl direction Suprathermal q	5:6:0	5:3:2	2:1:0	4:2:0	3:3:1	2:3:0
Strahl width	0:3:8	0:0:10	0:1:2	0:1:5	0:2:5	0:1:4
Strahl height	8:3:0	6:4:0	2:1:0	6:0:0	3:4:0	2:3:0
Total core beta	0:4:7	1:7:2	0:0:3	0:3:3	0:5:2	0:3:2
Magnitude of magnetic field	7:3:1	7:3:0	2:1:0	4:2:0	5:2:0	2:2:1

or positive correlation with rotation angle. The determination of correlation was made qualitatively. Here, the B angle is defined as

$$\Psi = \arccos(\hat{\mathbf{B}} \cdot -\hat{\mathbf{R}}). \quad (3)$$

$\hat{\mathbf{B}}$ is a unit vector in the magnetic field direction, and $-\hat{\mathbf{R}}$ is a unit vector pointing toward the Sun (opposite the radial vector).

For many of the figures in this paper, rather than showing all 42 days of data, we select a representative day (or multiple days) with data that trends consistent with those we saw in our statistical analysis, in order to illustrate the trends, we saw in our statistical analysis from Table 1.

3. Electron Velocity Distribution Function (eVDF)

Figure 1 shows the evolution of the eVDF with increasing magnetic field rotation angle (from Equation (3)) for 2020 October 2. The six different magnetic field rotation angles from a single day, as well as times of observation were chosen randomly for our analysis. First, we choose the smallest and largest magnetic field rotation angles for 2020 October 2 (one of the days of our observation), to represent the two extremes of magnetic field rotation angles. The smallest magnetic field rotation angle for the day was A (0.13°) and the largest magnetic rotation angle for the day was F (146.31°). Between the smallest and largest magnetic field rotation angles, we further subdivide the rotation angles for the day into four more magnetic field rotation angles (B, C, D, and E). We choose 15° , 30° , 90° , and 110° in order to cover a broad range of angles and display representative examples of how the eVDFs evolve with magnetic field rotation angles. Events B, C, D, and E represent times that matched this angle selection criterion.

Figure 2 shows a close-up view of only the antistrahl sides of the eVDFs from Figure 1. During a period with small magnetic field angle deflection (i.e., no switchback) (A), a deficit feature is seen on the antistrahl side of the eVDF. At larger magnetic

field rotation angles (inside switchbacks), the deficit feature on the antistrahl side of the eVDF is progressively filled in, and a larger suprathermal population is observed, as can be seen in Figure 2.

The eVDFs and fits from Figures 1 and 2 are obtained utilizing the analysis procedures developed by Halekas et al. (2020, 2021). We fit the eVDF measured by SPAN-E to a drifting bi-Maxwellian function to determine the characteristics of the core electron population, utilizing proton velocity measurements from PSP’s SPC to shift the eVDF into the solar wind reference frame, and magnetometer data (Bale et al. 2016) to orient the distribution with respect to the magnetic field. We rely on the assumption of the electron gyrotropy around the magnetic field, which should hold to a high degree in the plasma frame.

We account for secondary electron contamination from instruments and spacecraft surfaces by including an isotropic Maxwellian fit with a fixed temperature of 3.5 eV. We fit an anisotropic drifting bi-Maxwellian function simultaneously to represent the core electron population. The core fit covers an energy range of 6 eV to $4kT_0$ and encompasses all pitch angles, except for the 45° angle range surrounding the strahl direction of the eVDF.

Next, we add an isotropic Maxwellian to our core fits to capture the halo population. Like Halekas et al. 2020, we found there was no need to use a bi-Kappa function to fit the halo population, as our halo distributions were close to a Maxwellian, near the Sun’s environment. The halo fit covers measurements ranging from $4kT_c$ to 2000 eV and covers the same angular range as the core fit. Due to low counting statistics, the halo fit is not always successful, and thus halo parameter estimates do not exist at all times.

As an alternative way to capture the suprathermal populations, we compute the moments of the residual of the measured distributions with respect to the core fit (not core+halo as above), separated into field-aligned (FA) and anti-FA (AFA)

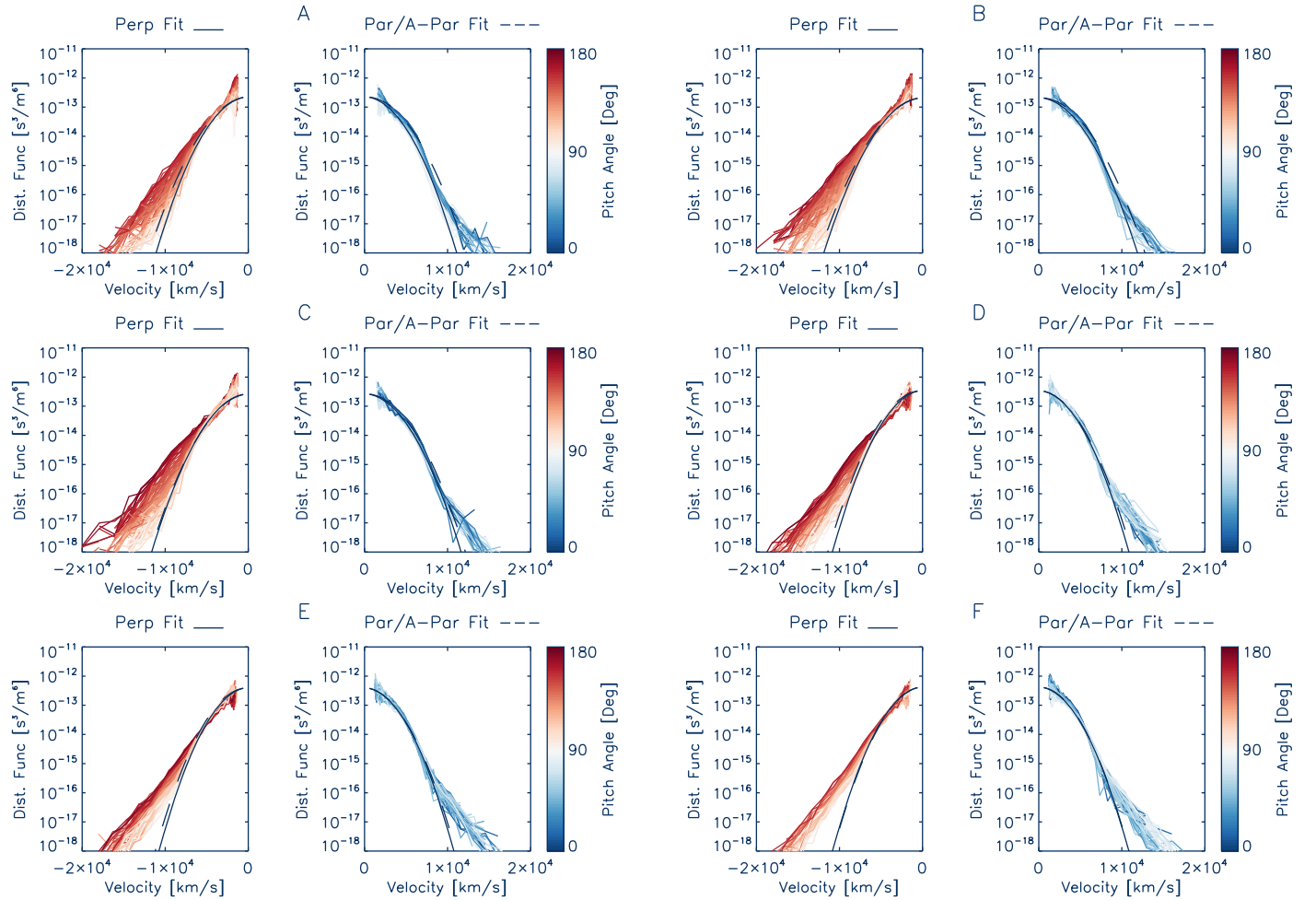


Figure 1. Evolution of the eVDF in the proton frame at six different times on 2020 October 2. Each eVDF plot corresponds to an increasing magnetic field rotation angle: (A) 0.13° [$11^{\text{h}}:34^{\text{m}}:47^{\text{s}}$], (B) 14.52° [$16^{\text{h}}:09^{\text{m}}:58^{\text{s}}$], (C) 28.81° [$12^{\text{h}}:59^{\text{m}}:22^{\text{s}}$], (D) 90.80° [$23^{\text{h}}:32^{\text{m}}:56^{\text{s}}$], (E) 110.54° [$23^{\text{h}}:18^{\text{m}}:08^{\text{s}}$], and (F) 146.31° [$23^{\text{h}}:12^{\text{m}}:26^{\text{s}}$]. The portions of the electron distribution with velocity components parallel to the B field (smaller pitch angles) are shown in blue. Those with antiparallel components (larger pitch angles) are in red, as shown by the color bar. The solid black lines and dashed lines in the panels are cuts through the fits in the perpendicular and parallel/antiparallel directions, derived as described below. During this period, the electron strahl flows in the antiparallel direction.

components, as in Halekas et al. (2021). This integrated residual density can be negative and corresponds to a deficit. This analysis utilizes electron gyrotropy to fill in some of the blocked portions of the FOV. Thus, these suprathermal parameters are not as subject to underestimation as the strahl-only parameters described above. Analogous to Halekas et al. (2021), we identify the sunward electron deficit by comparing the VDFs measured by SPAN-E to the drifting bi-Maxwellian fits to the core population described above.

To capture the strahl population, the remaining positive residuals of our measurements are integrated with respect to the superposition of our previous best-fit functions for energies above $4kT_c$ and pitch angles within 45° of the strahl direction. Strahl densities and heat fluxes are calculated by taking moments of this residual distribution function. The integrated density of the residual can be negative which corresponds to a deficit. Unlike the core and halo parameters, the strahl electrons are subject to underestimation due to the presence of FOV gaps and obstruction of the spacecraft. Lack of strahl population capture is also mentioned in Section 4 of this paper.

Looking at the eVDF panels (A) and (B) in Figure 2, a deficit appears as a negative residual and falls below the drifting bi-Maxwellian core fit. At moderate velocities, the antistrahl

portion of the eVDF drops below the core fit before rising above the fit at high velocities. At larger magnetic field rotations (panels (E) and (F) in Figure 2), the deficits observed on the antistrahl side are filled, and we do not observe the negative residuals. As discussed by Halekas et al. (2021) the rise of the electron distribution above the core fit at higher velocities may be due to the presence of a weak halo population. The instrument background can be an issue for both the core deficit and the halo. However, since the background (constant in count rate, and thus falling as $1/E^2$ in distribution function) falls much less rapidly than the actual VDF, its effects become progressively more important at higher energies. Thus, at a few thermal speeds where the cutoff occurs, the background is not too significant. However, at higher energies (many thermal speeds), the background becomes more appreciable, and can even be dominant in the highest energy bins. Instrumental background counts from penetrating cosmic rays and natural radioactivity in the microchannel plate detectors also contribute. During all measurements, the SPAN-E attenuator is engaged, which increases the relative effect of the background, since the ambient electrons are reduced in flux, but the background sources are not.

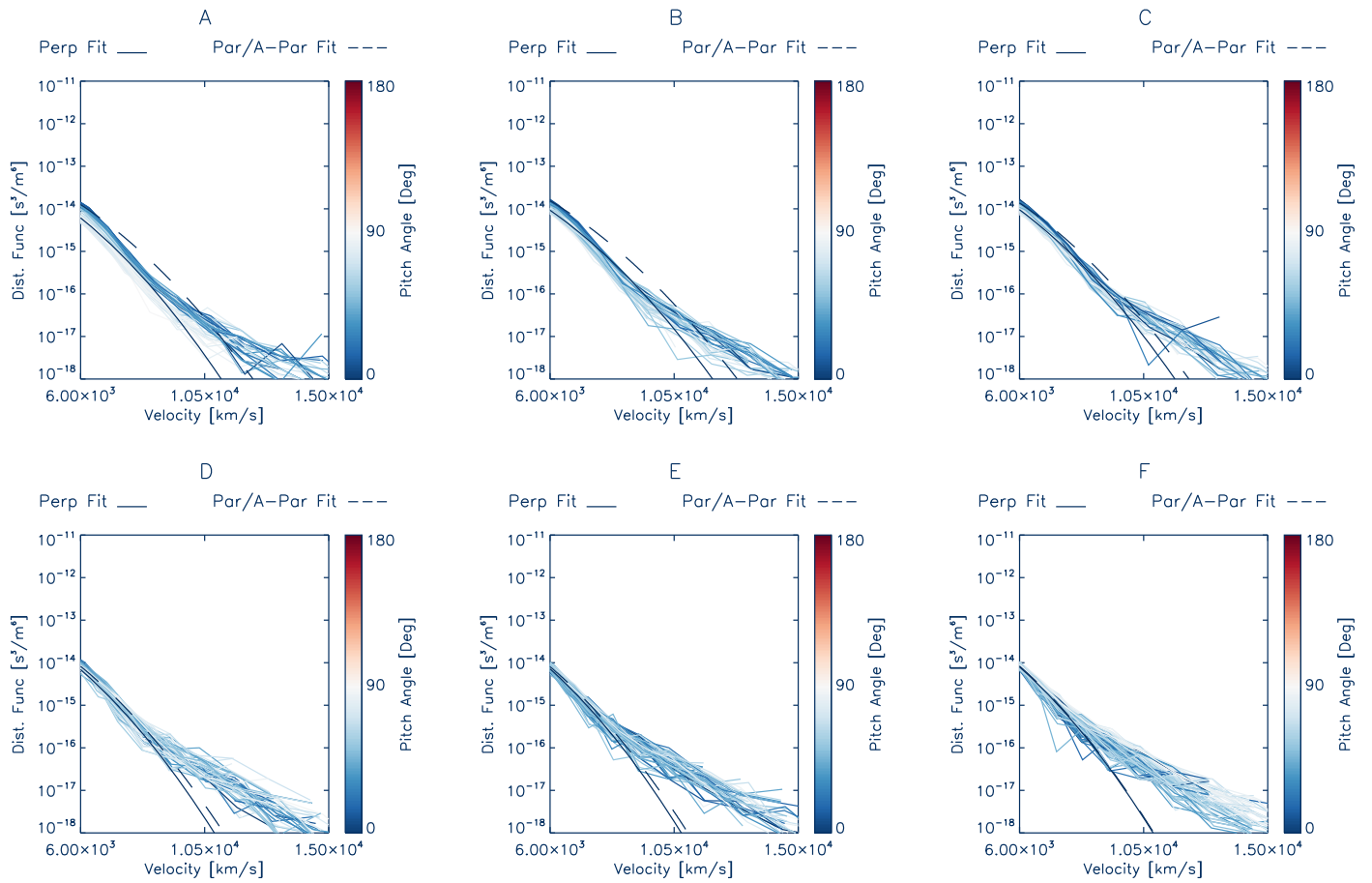


Figure 2. Close-up view of the antistrah side of the eVDFs from Figure 1 for 2020 October 2. Like Figure 1, each eVDF plot corresponds to an increasing magnetic field rotation angle: (A) 0.13° , (B) 14.52° , (C) 28.81° , (D) 90.80° , (E) 110.54° , and (F) 146.31° . The portions of the electron distribution with velocity components parallel to the B field (small pitch angles) are shown in blue.

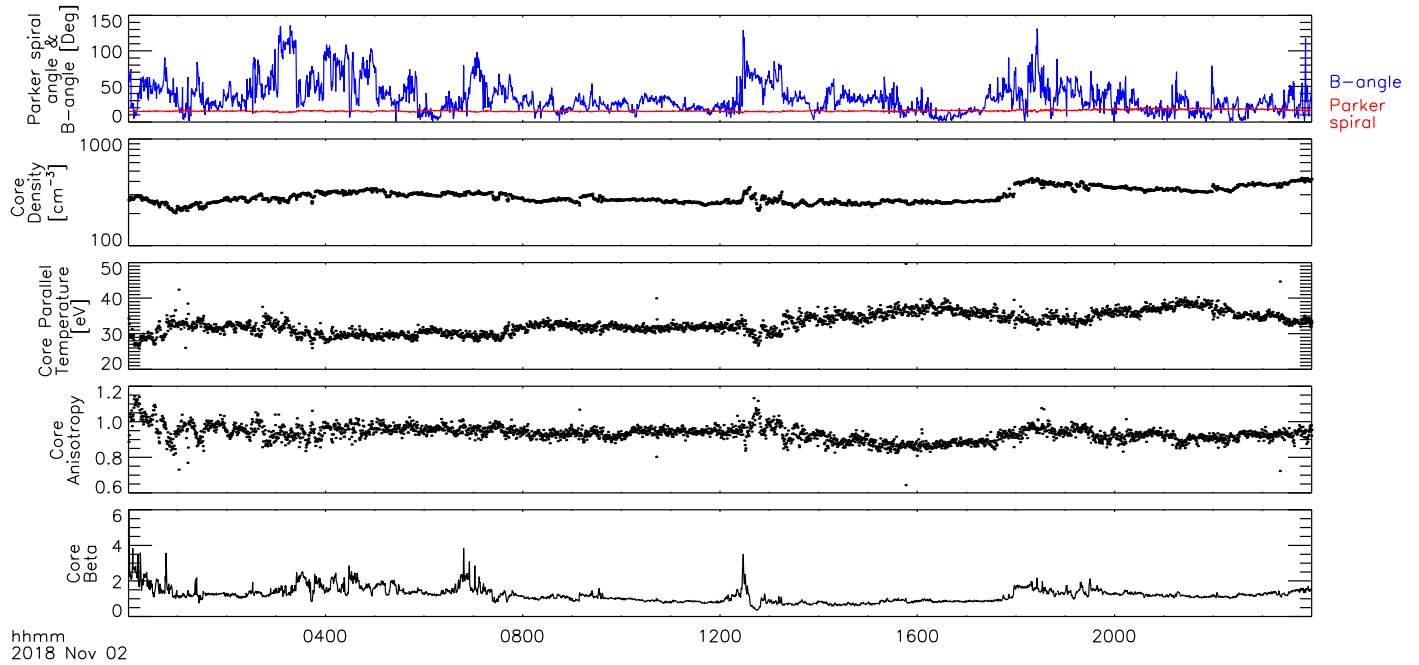


Figure 3. Various core electron parameters plotted as a function of time for 2018 November 2. From top to bottom: Magnetic field rotation angle/B angle (degrees) and nominal Parker spiral angle (degrees), core number density (per cubic centimeter), core parallel component temperature (electronvolts), core anisotropy, and core electron plasma beta.

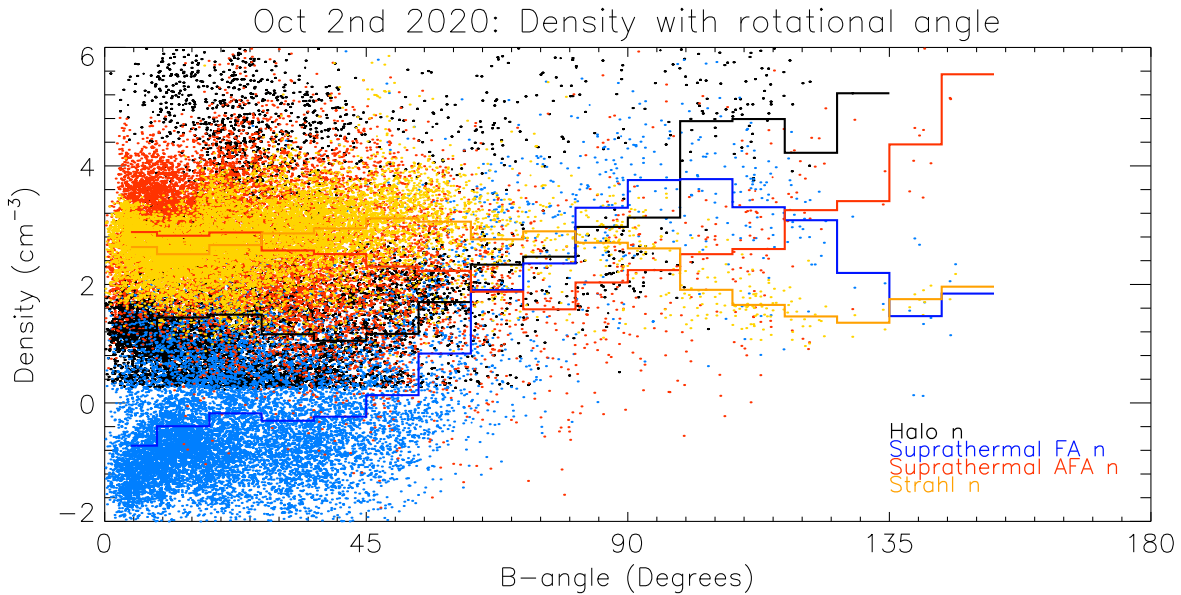


Figure 4. Scatterplot of the number density (n) for the strahl, halo, suprathermal FA (antistrah direction), and suprathermal AFA (strahl direction) populations, with their respective averages, in relation to magnetic field rotation angle for 2020 October 2. Each dot on the plot represents an individual measurement point.

On the strahl side of the eVDF in Figure 1, the electron distribution is always above the core fit, due to the presence of strahl electrons. Due to spacecraft obstructions, a portion of the strahl electron population is not measured for the smallest (A) and largest (F) magnetic field rotation angles. Thus, any trends in the strahl parameters at small/large magnetic field rotation angles should be taken with caution.

4. Core Parameters

We next investigate the electron parameters statistically, starting with the core electrons. Our results from Figure 3 reveal no clear changes in most core electron parameters with magnetic field direction, at least within this day. Investigating these parameters further on other dates, we find no consistent dependence of the core parallel temperature (see Table 1) or core anisotropy on the magnetic field rotation angle. We do find an increase in the core densities at a larger magnetic field rotation angle on some days (16 out of 42 days of our observations) that we analyzed. However, we find no significant change in the core number densities with the magnetic field rotation angle on other days. Table 1 summarizes all the observations of the core parameters for six PSP encounters.

5. Suprathermal (Halo and Strahl Electrons)

Next, we investigate the suprathermal (strahl + halo) populations and their relationship to magnetic field rotation angle. In Figure 4, the densities of the suprathermal populations (derived as described in Section 3) are plotted with respect to the angle of rotation of the magnetic field from radial. One of the most striking changes we observe is the FA suprathermal density trend from negative to positive values with increasing magnetic field rotation angle (As shown in Table 1, we see a similar trend on 35 out of 42 days studied.) This trend agrees with features observed in the individual eVDFs (Figure 2). It indicates a possible trend of suprathermal density in the antistrah direction transitioning from a deficit at low magnetic field rotation angles (i.e., outside of switchbacks) to a surplus at

higher magnetic field rotation angles (i.e., inside switchbacks). Additionally, we also observe the halo density increasing with magnetic field rotation angle, on many days of our observation (27 out of 42 days). Based on the observed increase in both FA suprathermal and halo densities, we speculate that the growth of the suprathermal halo may refill the FA suprathermal deficits. Given the presence of the sunward deficit corresponds to a net dearth of suprathermal electrons (with respect to a Maxwellian), while the presence of the halo corresponds to a net surplus, formation of the halo erasing the sunward deficit is a possible hypothesis. The observed correlation between the suprathermal halo and FA suprathermal deficit, could also be explained by multiple mechanisms in play. When PSP crosses the HCS, the polarity of the strahl is reversed, and the strahl is on the FA side rather than the AFA side of the distribution.

Commensurate with the increase of FA suprathermal density, we also found an increase in the halo number density with magnetic field rotation angle. Figure 4 shows that the halo electron population increases as the FA suprathermal density changes from a deficit to excess, suggesting that these two trends may be related. This also suggests that the processes that produce the halo may also remove deficits in the antistrah portion of the eVDF. Halekas et al. (2021) reported similar trends in the solar wind close to the Sun. This work seems to reinforce those previous results and may suggest that these processes may occur preferentially and/or to a higher degree in switchbacks. On the other hand, the AFA suprathermal density shows no consistent trends (see Table 1). We could not see a consistent pattern when comparing AFA suprathermal density between days of our observation. Hence, it is difficult for us to make any form of a deduction from AFA suprathermal density for the time being.

We caution the reader that apparent deviations from the mainstream trend may be due to a lack of data points at very large rotation angles. On the other hand, partial obstructions of PSP's FOV in the sunward direction may affect the results at the smallest rotation angles.

With the increase in suprathermal density in the FA direction, we would anticipate a corresponding increase in

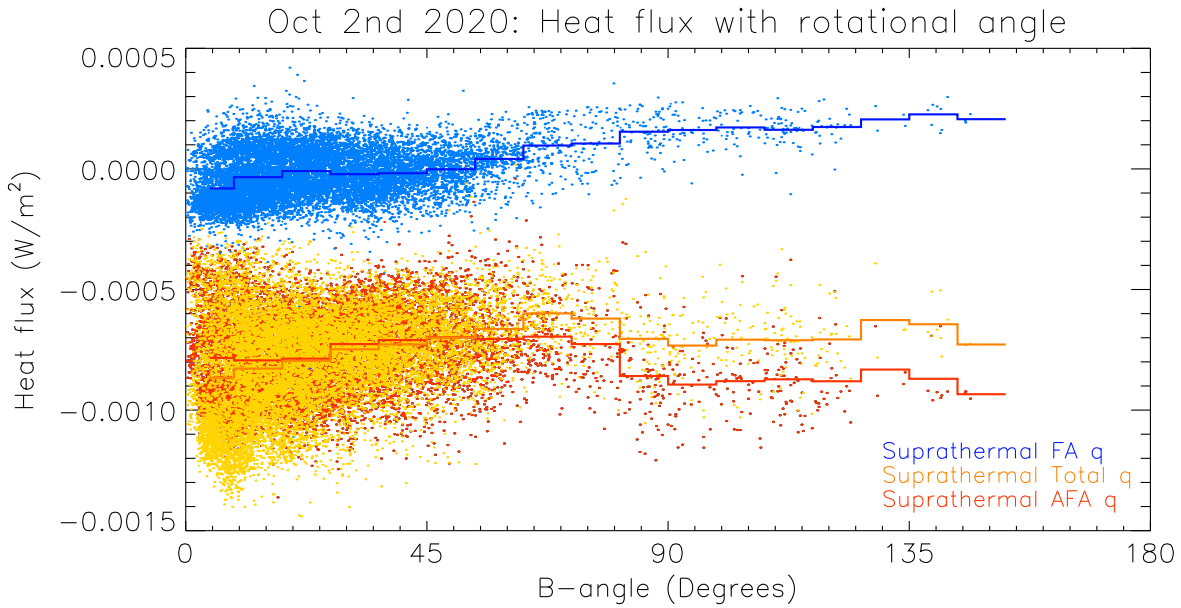


Figure 5. Scatterplot of the heat flux(q) for the FA suprathermal (blue), AFA suprathermal (red), and suprathermal total (FA + AFA) (orange) populations, with their respective averages. FA suprathermal heat flux goes from a deficit to excess, while AFA heat flux decreases slightly at large magnetic field rotation angles. Total heat flux shows an anticorrelation with magnetic field rotation angle, primarily due to the FA contribution.

heat flux in that direction (Halekas et al. 2020). In Figure 5, we find an increase in heat flux in the FA direction of the magnetic field. The FA heat flux increases from a negative value to a positive value with increasing magnetic field rotation angle (34 out of 42 days). This trend again possibly suggests that suprathermal electrons fill in the deficits on the antistrahl side of the eVDF from Figure 1 at larger magnetic field rotation angles.

Looking at the total heat flux (FA + AFA heat flux) of the suprathermal electrons, on many days of our analysis, including the one in Figure 5, we observe a decrease in the magnitude of the total heat flux with switchback rotation angle. The overall negative value of the total heat flux indicates that most of the electron heat flux is carried by the strahl electrons (as expected), which is antiparallel to the magnetic field on this date. At larger magnetic field rotation angles, the magnitude of the suprathermal electron heat flux decreases. This decrease is due to the increase of the FA suprathermal electron heat flux with increasing magnetic field rotation angle. We speculate that at larger magnetic field rotation angles (i.e., inside switchbacks), heat carrying suprathermal populations are becoming more isotropic, due to the commensuration of possible growth of the halo population (as can be seen in Figure 4). One possible explanation for these observations is that some process that occurs in switchbacks may help form a halo population. This halo population in turn fills in the deficits of the FA electron distribution and so, we see an increase in both density and heat flux in the antistrahl direction. Hence, we see a possible correlation between the trends we saw in both Figures 4 and 5. As previously stated, this is just a possible hypothesis worth noting in our observations. Other unknown mechanisms could play a part in our observed trends. The AFA suprathermal electron heat flux stayed relatively constant with ever-increasing magnetic field rotation, suggesting that not much change occurs on the AFA portion of the eVDF.

We now focus our attention on the AFA portion of the eVDF, which on this date contains the strahl. In Figure 4, it can be seen that the strahl number density stayed relatively

unchanged, with increasing magnetic field rotation angle. On many days of our observation, the strahl number densities do not show a consistent trend with increasing magnetic field rotation (see Table 1). The AFA portion of the eVDF from Figure 1 also does not show a consistent pattern when comparing eVDF from multiple days. We expected the strahl number density to decrease with increasing halo number density, but our observations do not reveal a conclusive connection between the halo and strahl densities.

Some possible reasons why we do not see the strahl number density changing with increasing magnetic field rotation angle include the resolution of the strahl measurements. A poor angular resolution of the strahl may result in not seeing much scattering of the strahl population into a halo population. Alternatively, there may not be a connection between halo electron formation and strahl scattering. To reemphasize this observation and show its consistent occurrence, we plot the FA suprathermal number density with the associated heat flux, as a function of magnetic field rotation angle for various selected days, as can be seen in Figure 6. From Figure 6, two trends are apparent. First, the number density of the FA suprathermal population shows a positive correlation with the rotation of the magnetic field, with a trend from negative to positive values, which agrees with the results shown in Figure 4. Second, the associated heat fluxes also become more positive with a larger magnetic field rotation angle, in agreement with the results shown in Figure 5. These observations seem to support and extend the results shown in Figures 4 and 5 and may indicate that the sunward suprathermal deficit is consistently filled in at larger magnetic field rotation angles, resulting in a transition from negative to positive sunward heat flux.

From Figure 4, the strahl number density remained relatively unchanged as a function of the magnetic field rotation angle. This observation is puzzling, since it does not obviously support the theory of strahl electrons being scattered into the halo. Figure 7 shows the strahl distribution angular width and height plotted with respect to the switchback rotation angle. Our results suggest that at larger switchback angles, the height

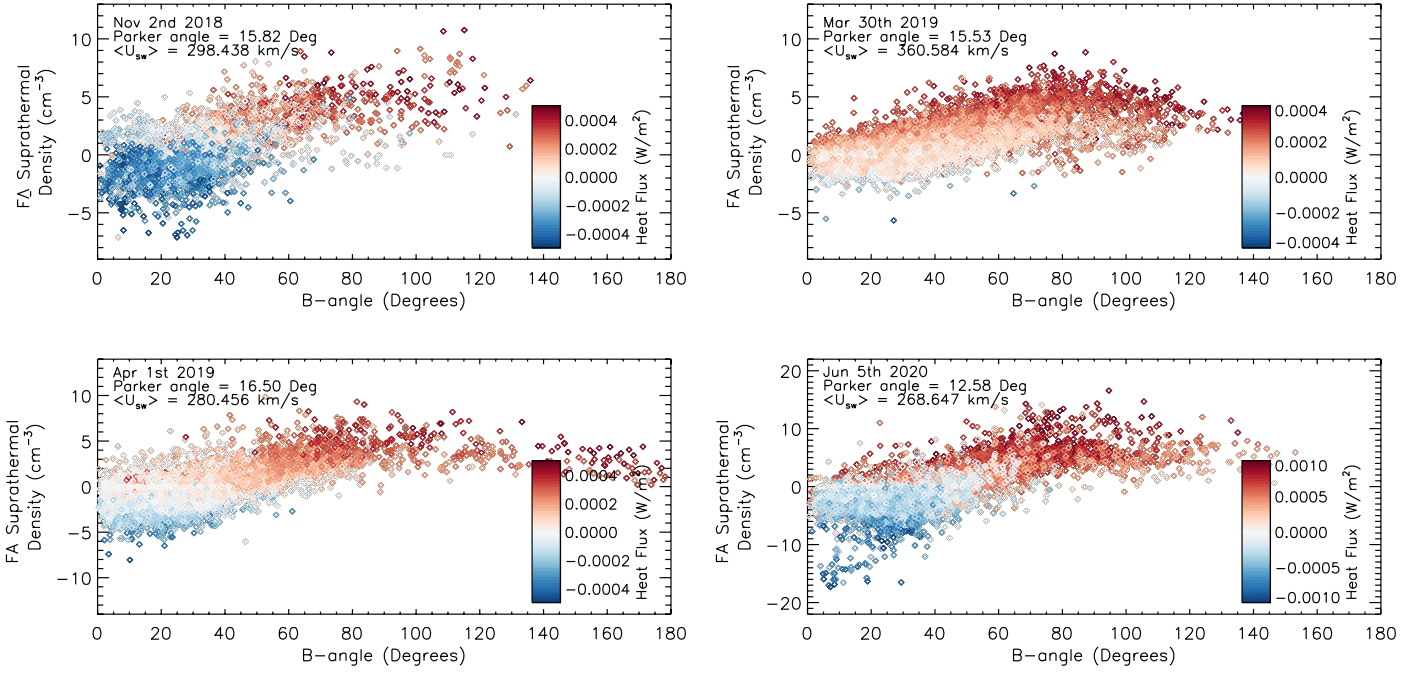


Figure 6. Scatterplots of the FA suprathermal number density and heat flux for selected dates. The color of each data point represents the heat flux, with positive (FA) heat flux shown in red and negative (AFA) in blue. Both the FA number density and heat flux become positive at larger magnetic field rotation angles. Nominal Parker spiral angle and the average solar wind speed are also listed for each day.

(amplitude) of the strahl distribution decreases (27 out of 42 days), and the strahl distribution width increases (34 out of 42 days). In Figure 4, we did not see a clear picture of strahl number density changing with magnetic field rotation. However, our results may indicate that while the number density of the strahl (area under the distribution curve) does not change appreciably, the shape of the strahl distribution function does. Thus, our results may indicate that at larger magnetic field rotation angles (i.e., inside switchbacks), the strahl distribution function evolves to become more spread out. This observation could explain why we do not see significant changes in the average strahl density in Figure 4, but this is an early speculation.

Halekas et al. (2021) found that deficits in the inner heliosphere tend to occur preferentially in plasma with low electron beta (β), low collisional age (A_e) plasma, and a more anisotropic ($T_{\text{perp}}/T_{\text{par}}$) electron core population. When large halo populations are observed, the opposite set of circumstances holds. These results motivate us to investigate the plasma content inside switchbacks and identify whether similar trends can be seen. In Figure 8, we plot the total electron core plasma beta ($\beta_c = 2\mu_0 n_c k_B T_c / B^2$) and its components with respect to increasing magnetic field rotation for 2018 November 5. Both components of the plasma beta appear correlated with magnetic field rotation angle (core beta total: 19 out of 42 days).

We now investigate the possible cause of the core electron beta parameter increase. We find no clear changes in the electron core temperature with magnetic field rotation angle, in agreement with the overall trend shown in Figure 3 (see Table 1). As previously stated, while we do see some correlation between the core densities and magnetic field rotation angle on some days, we find even more significant changes in the magnitude of the magnetic field. On many days of our observation (27 out of 42 days), the magnitude of the magnetic field decreases with larger magnetic field rotation

angles. Thus, the increase in plasma beta results mainly from the decrease in the magnitude of the magnetic field with magnetic field rotation angle. These results may indicate that the plasma is at least partly compressible rather than purely Alfvénic.

6. Discussion and Conclusion

We have analyzed the trends in the eVDF from small magnetic field rotation angles (outside switchbacks) to high magnetic field rotation angles (inside switchbacks). Our results show that, on average, the deficit features in the FA (antistrahl) portion of the eVDF gradually disappear, and the antistrahl suprathermal flux increases, as the magnetic field rotation angle increases. In the AFA portion (strahl side) of the eVDFs, on the other hand, we find no consistent trends (see Table 1).

With the increase in FA suprathermal densities, our data also seem to show the halo population increasing, suggesting halo electrons may be responsible for the observed increasing FA densities and eventually erasing deficit feature in eVDFs. As mentioned several times in this paper, this is just one possible theory that could explain the trends we observed. We did not see a clear pattern in the strahl density as a function of the magnetic field rotation angle. Observations of both the FA and AFA electron distributions align with the trends we saw in the eVDFs.

We also found that the FA heat flux had an increasing trend (from a negative to a positive value) with increasing magnetic field rotation angles, further supporting the theory that deficit features in the eVDF may be erased by halo electrons. The magnitude of the total heat flux of the suprathermal population also decreased, as a result of the increase in FA heat flux. As expected, most of the heat flux in the electron population resides in the AFA portion of the eVDF (large heat flux magnitude), which is dominated by the strahl population.

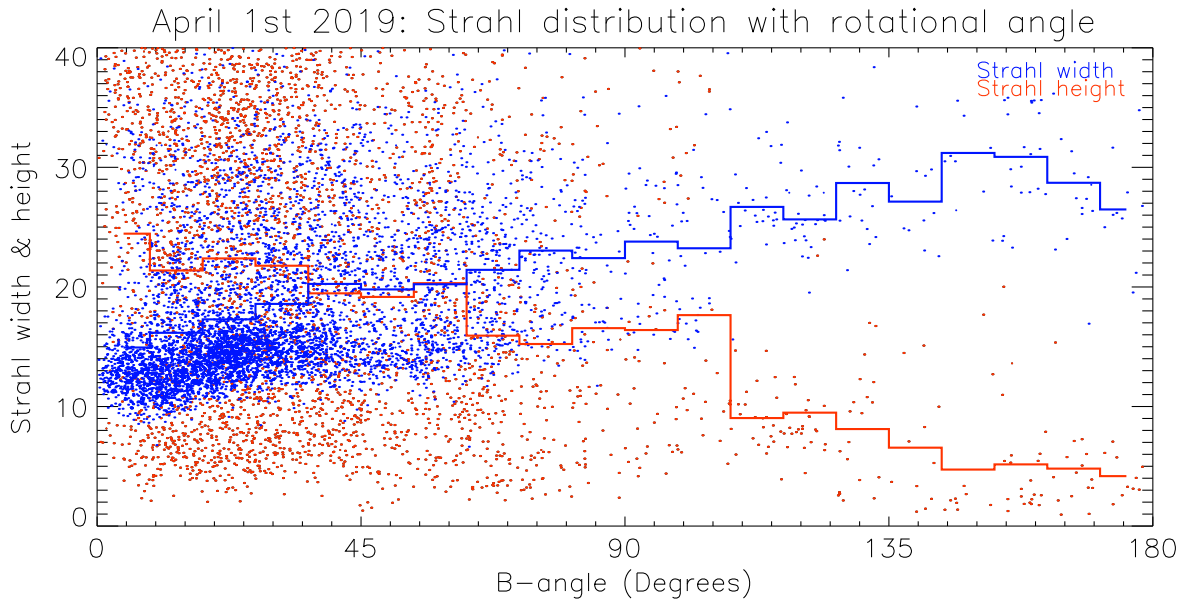


Figure 7. Strahl distribution width and height from a Gaussian fit to the pitch angle distribution measured at 314 eV, as a function of magnetic field rotation angle, for 2019 April 1. The height of the Gaussian is the amplitude of the curve. The strahl height is dimensionless as the amplitude of the strahl is normalized to the magnitude of the distribution at 90° angle. The strahl width represents the standard deviation of the Gaussian and is in units of degrees.

To explore the lack of a clear trend in strahl number density, we investigated the strahl shape at constant energy by fitting a Gaussian function. We found that the angular height of the strahl distribution at 314 eV decreases, but its angular width increases, with increasing magnetic field rotation angle. The broadening of the strahl electron distribution may indicate that strahl electrons are increasingly scattered at greater magnetic field rotation angles. This observation may support the idea that electrons can be scattered to form the halo inside switchbacks, as seen elsewhere in the solar wind (Kajdic et al. 2016; Berčič et al. 2019).

Finally, our results show that the electron core beta parameter increases with magnetic field rotation angle during many time periods. Our data indicate that the electron core temperature and number density have no clear and consistent trends with magnetic field rotation angles. However, we find an average anticorrelation between the magnitude of the magnetic field and its rotation angle, which leads to the increase in the electron beta. These results indicate that the plasma may be partly compressible, suggesting that switchbacks can exhibit some fast magnetosonic-like properties instead of remaining purely Alfvénic.

We will now discuss our observations and describe the implications of our results. Krasnoselskikh et al. (2020) pointed out that a purely Alfvénic structure would exhibit relatively constant magnetic field magnitude, with strong coupling of magnetic field and velocity perturbations during the same period. Our results did not indicate a constant magnetic field magnitude. Instead, our results indicate some variation of the magnetic field magnitude as a function of magnetic field rotation. On the other hand, during events of compressible-like features, Krasnoselskikh et al. (2020) report a considerable ion beta value during switchback events. Their observations appear largely consistent with ours, since our data show a larger electron beta, at larger magnetic field rotation angles. They also report a significantly smaller magnitude of magnetic field inside these compressible-like structures than outside, which is also in agreement with our observations. On the other hand,

Krasnoselskikh et al. (2020) reported an ion temperature increase inside compressible switchback structures, while the ion number density decreased simultaneously. We did not find a similar trend in the electrons. Instead, our results indicate that the electron temperature on average remains relatively unchanged, while the electron core density either increases or remains relatively unchanged. This observation suggests, that, though both results are consistent with fast magnetosonic-like modes, the variation of the electron temperature may differ from that of the ions inside switchbacks. Woolley et al. (2020) found the magnitude of the B field slightly increased during switchback periods, and this increase was balanced by a decrease in core proton density. Thus, the core proton beta parameter remained relatively unchanged during switchback periods and exhibited more of an Alfvénic-like nature. This suggests that switchbacks can exhibit both Alfvénic-like and compressible-like tendencies, as mentioned by Krasnoselskikh et al (2020). Meanwhile, Zank et al. (2020) reported that all three magnetic field components (radial, tangential, and normal) changed during switchback periods, as compared to the background plasma. Additionally, proton number density and proton temperature showed significant changes during switchback periods, while the magnetic pressure ($B^2/2\mu_0$) stayed relatively unchanged. These trends lead to a proton beta that increases during the switchback periods, similar to our result for the electron beta, though possibly due to a different combination of factors. Given these results, Zank et al. (2020) concluded that switchbacks are not purely Alfvénic structures but are instead compressible fast magnetosonic structures propagating close to Alfvén speed.

Larosa et al. (2021) performed a statistical analysis that indicated higher proton beta inside switchbacks, and observed that approximately a quarter of the switchbacks they sampled exhibited compressible-like behavior. Furthermore, a significant portion of switchbacks had a smaller average magnetic field magnitude inside of switchbacks compared to outside of switchbacks. They also noted that proton densities inside switchbacks could increase or decrease and typically differed

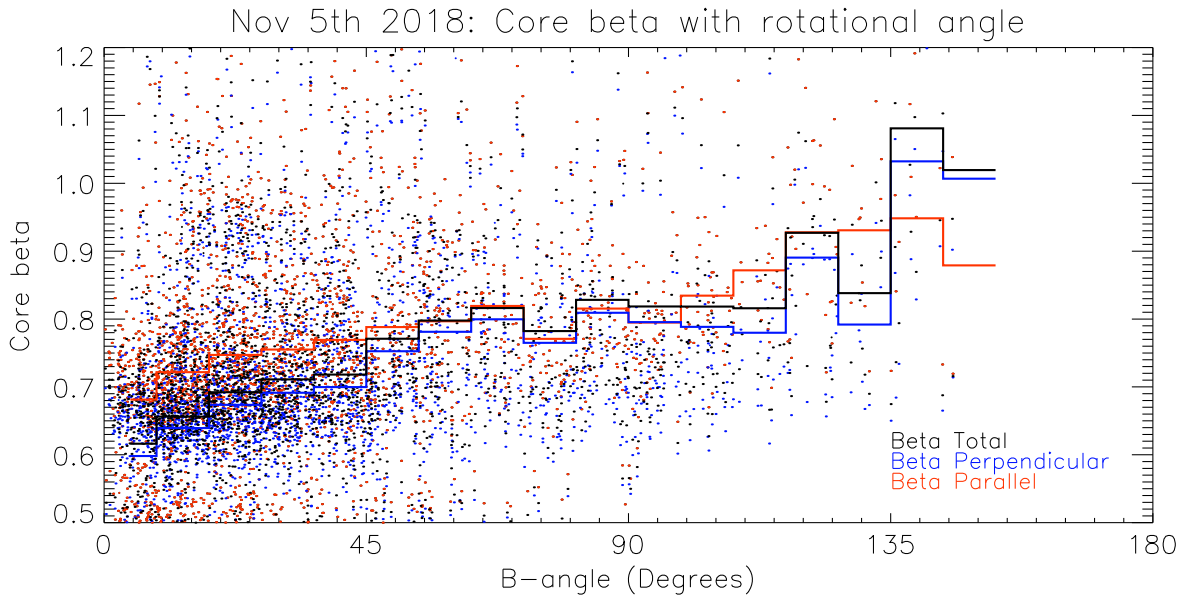


Figure 8. Core electron plasma beta correlation to the rotation of the magnetic field for 2018 November 5. Results show a direct correlation between the beta parameter and magnetic field rotation angle.

from the background value. Though density changes were observed in individual switchback events, the average proton density remained constant. Our data shows a similar trend, with the core densities remaining relatively constant on many days of our observations. Our results therefore appear largely consistent with previous work, and support the theory that not all switchbacks have purely Alfvénic structures.

Utilizing Helios spacecraft measurements, Berčič et al. (2019) reported scattering of the strahl electrons between 0.3 and 1 au, and found that the strahl distribution is much broader in high (>0.4) electron core beta solar wind. Inside 0.3 au, Cattell et al. (2021) used PSP observations to identify enhanced scattering when the parallel component of the electron beta was greater than 1. Both Figures 6 and 7 seem to support these findings. At high beta values, the strahl distribution function is much broader. Berčič et al. (2019) also found that the scattering of electrons is very efficient over a large (between 200 and 500 eV) energy range, especially in a high electron core beta regime.

Berčič et al. (2019) also noted the possible generation of whistler-mode waves in high beta solar wind. These predominantly anti-sunward waves, which may be generated by a heat-flux instability (Gary et al. 1975), could scatter the strahl and isotropize the suprathermal population through resonance interactions to form the halo (Vocks & Mann 2003; Vocks et al. 2008; Vocks 2012). Kajdic et al. (2016) utilized observations from the Cluster spacecraft mission close to 1 au to show that narrowband whistler waves significantly increase the pitch angle distribution of the suprathermal electrons. All these whistler waves were observed during periods of slow solar wind (large plasma beta), and strahl broadening occurred at various electron energy values (with the most significant strahl broadening occurring at around 344 eV). The ratio of strahl to halo flux ($F_{\text{strahl}}/F_{\text{halo}}$) was also closer to unity in the presence of whistler-mode waves.

At a heliocentric distance of ~ 0.2 – 0.3 au, narrowband whistler-mode waves have been found to occur frequently (Cattell et al. 2021). During intervals of whistler-mode interactions, electron pitch angle distributions centered at 314

and 204 eV were found to broaden significantly. Furthermore, these waves primarily occurred during periods of large magnetic field variability, reduced magnetic field magnitudes, and within or at the boundaries of switchbacks. All these observations may indicate that the electron distribution evolution we observe could result from interaction with whistler-mode waves.

In a more recent study, electron densities and magnetic fields measured at 0.3 au and with whistler-mode parameters have been modeled to examine the interactions between electrons and whistler-mode waves (Cattell & Vo 2021). By tracking particle motion from the simulation, waves at various angles were found to energize the electron populations, produce multiple resonant interactions, and develop strong scattering processes. These interactions strongly scatter the strahl distribution and produce hotter halo populations.

The enhanced wave activity observed during periods of switchbacks (Agapitov et al. 2020; Krasnoselskikh et al. 2020; Mozer et al. 2020; Larosa et al. 2021) suggest that wave-particle interactions may not only play a part in the scattering of the strahl electron population but may also play a key role in the formation of the halo. Boundaries of switchbacks are also known to have high wave activities (Agapitov et al. 2020; Krasnoselskikh et al. 2020; Mozer et al. 2020; Larosa et al. 2021), suggesting another possible location for studying heat-flux instability and formation of whistler-mode waves that scatter strahl to the halo.









To summarize our results, we found that the eVDF observed at larger magnetic field rotation angles (inside switchbacks), differs from that observed at smaller magnetic field rotation angles (outside switchbacks). Both the halo and antistrahl suprathermal densities increase with greater magnetic field rotation angle, suggesting that the halo may fill in the sunward deficit. The strahl distribution also has a greater angular spread at large magnetic field rotation angles. All these observations suggest that enhanced scattering takes place inside switchbacks. Given the frequent occurrence of switchbacks close to the Sun, switchbacks may play an important role in the

evolution of the solar wind electrons between the corona and the outer heliosphere.

Further work should include a more detailed investigation of the electron core beta inside switchbacks and possible connection to wave-particle interactions. We also wish to understand the relationship between the structure and evolution of the strahl distribution and the occurrence of whistler-mode waves as a function of radial distance from the Sun. Finally, future investigations should focus on the origin of the increase in the antistrahl suprathermal population. Our results reveal no clear change in the strahl density; thus, the electron contribution to the halo population may come from elsewhere in the distribution.

We acknowledge the NASA/SWEAP contract NNN06AA01C for the support of this work.

ORCID iDs

Raaman Nair  <https://orcid.org/0000-0002-1964-5883>
 Jasper S. Halekas  <https://orcid.org/0000-0001-5258-6128>
 Phyllis L. Whittlesey  <https://orcid.org/0000-0002-7287-5098>
 Davin E. Larson  <https://orcid.org/0000-0001-5030-6030>
 Roberto Livi  <https://orcid.org/0000-0002-0396-0547>
 Justin C. Kasper  <https://orcid.org/0000-0002-7077-930X>
 Anthony W. Case  <https://orcid.org/0000-0002-3520-4041>
 Michael L. Stevens  <https://orcid.org/0000-0002-7728-0085>
 Stuart D. Bale  <https://orcid.org/0000-0002-1989-3596>
 Robert J. MacDowall  <https://orcid.org/0000-0003-3112-4201>
 Marc P. Pulupa  <https://orcid.org/0000-0002-1573-7457>

References

Agapitov, O. V., Dudok de Wit, T., Mozer, F. S., et al. 2020, *ApJL*, **890**, L20
 Bale, S. D., Badman, S. T., Bonnell, J.W., et al. 2019, *Natur*, **576**, 237
 Bale, S. D., Goetz, K., Harvey, P. R., et al. 2016, *SSRv*, **204**, 49
 Bale, S. D., Pulupa, M., Salem, C., et al. 2013, *ApJL*, **769**, L22
 Balogh, A., Forsyth, R. J., Lucek, E. A., et al. 1999, *GeoRL*, **26**, 631
 Berčić, L., Larson, D., Whittlesey, P., et al. 2020, *ApJ*, **892**, 88
 Berčić, L., Maksimovic, M., Halekas, J. S., et al. 2021, *ApJ*, **921**, 83
 Berčić, L., Maksimović, M., Landi, S., et al. 2019, *MNRAS*, **486**, 3404
 Boldyrev, S., & Horaites, K. 2019, *MNRAS*, **489**, 3412
 Borovsky, J. E. 2016, *JGRA*, **121**, 5055
 Case, A. W., Kasper, J. C., Stevens, M. L., et al. 2020, *ApJS*, **246**, 43
 Cattell, C., Short, B., Breneman, A., et al. 2021, *A&A*, **650**, A8
 Cattell, C., & Vo, T. 2021, *ApJL*, **914**, L33
 Chang, Q., Xu, X., Xu, Q., et al. 2019, *ApJ*, **884**, 102
 Cuperman, S., Harten, A., & Dryer, M. 1972, *ApJ*, **177**, 555
 Dudok de Wit, T., Krasnoselskikh, V. V., Bale, S. D., et al. 2020, *ApJS*, **246**, 39
 Fedorov, A., Louarn, P., Owen, C. J., et al. 2021, *A&A*, **656**, A40
 Feldman, W. C., Asbridge, J. R., Bame, S. J., et al. 1975, *JGR*, **80**, 4181
 Fox, N. J., Velli, M. C., Bale, S. D., et al. 2016, *SSRv*, **204**, 7

Gary, S. P. 1978, *JPIPh*, **20**, 47
 Gary, S. P., Feldman, W. C., Forslund, D. W., et al. 1975, *JGR*, **80**, 4197
 Gary, S. P., Scime, E. E., Phillips, J. L., et al. 1994, *JGR*, **99**, 23391
 Gary, S. P., Skoug, R. M., & Daughton, W. 1999, *PhPI*, **6**, 2607
 Graham, G. A., Rae, I. J., Owen, C. J., et al. 2017, *JGRA*, **122**, 3858
 Guo, Y., Thompson, P., Wirzburger, J., et al. 2021, *AcAau*, **179**, 425
 Halekas, J. S., Berčić, L., Whittlesey, P., et al. 2021, *ApJ*, **916**, 16
 Halekas, J. S., Whittlesey, P., Larson, D. E., et al. 2020, *ApJS*, **246**, 22
 Hollweg, J. V. 1974, *JGR*, **79**, 3845
 Horaites, K., Astfalk, P., Boldyrev, S., et al. 2018, *MNRAS*, **480**, 1499
 Horaites, K., Boldyrev, S., & Medvedev, M. V. 2019, *MNRAS*, **484**, 2474
 Horbury, T. S., Matteini, L., & Stansby, D. 2018, *MNRAS*, **478**, 1980
 Innocenti, M. E., Boella, E., Tenerani, A., et al. 2020, *ApJL*, **898**, L41
 Kajdič, P., Alexandrova, O., Maksimovic, M., et al. 2016, *ApJ*, **833**, 172
 Kasper, J. C., Abiad, R., Austin, G., et al. 2016, *SSRv*, **204**, 131
 Kasper, J. C., Bale, S. D., & Schwadron, N. A. 2019, *Natur*, **576**, 228
 Korh, H., Rastätter, L., Anderson, B. J., et al. 2011, *AnGeo*, **29**, 1809
 Krasnoselskikh, V., Larosa, A., Agapitov, O., et al. 2020, *ApJ*, **893**, 93
 Landi, S., Hellinger, P., & Velli, M. 2006, *GeoRL*, **33**, L14101
 Landi, S., Matteini, L., & Pantellini, F. 2012, *ApJ*, **760**, 143
 Larosa, A., Krasnoselskikh, V., Dudok de Wit, T., et al. 2021, *A&A*, **650**, A3
 López, R. A., Lazar, M., Shaaban, S. M., et al. 2020, *ApJL*, **900**, L25
 Maksimovic, M., Pierrard, V., & Lemaire, J. F. 1997, *A&A*, **324**, 725
 Maksimovic, M., Zouganelis, I., Chaufray, J.-Y., et al. 2005, *JGRA*, **110**, A09104
 Matteini, L., Horbury, T. S., Neugebauer, M., et al. 2014, *GeoRL*, **41**, 259
 McManus, M. D., Bowen, T. A., Mallet, A., et al. 2019, *ApJS*, **246**, 67
 Meng, M.-M., Liu, Y. D., Chen, C., et al. 2022, *RAA*, **22**, 035018
 Meyer-Vernet, N. 2007, *Basics of the Solar Wind*, Cambridge Atmospheric and Space Science Series (1st ed.; Cambridge: Cambridge Univ. Press)
 Micera, A., Zhukov, A. N., López, R. A., et al. 2020, *ApJL*, **903**, L23
 Mozer, F. S., Agapitov, O. V., Bale, S. D., et al. 2020, *ApJS*, **246**, 68
 Mozer, F. S., Bale, S. D., Bonnell, J. W., et al. 2021, *ApJ*, **919**, 60
 Parker, E. N. 1958, *ApJ*, **128**, 664
 Pilipp, W. G., Miggenrieder, H., Montgomery, M. D., et al. 1987, *JGRA*, **92**, 1075
 Roberg-Clark, G. T., Drake, J. F., Swisdak, M., et al. 2018, *ApJ*, **867**, 154
 Rosenbauer, H., Schwenn, R., Marsch, E., et al. 1977, *JGZG*, **42**, 561
 Saeed, S., Sarfraz, M., Yoon, P. H., et al. 2017, *MNRAS*, **465**, 1672
 Saito, S., & Gary, S. Peter 2007, *GeoRL*, **34**, L01102
 Salem, C., Hubert, D., Lacombe, C., et al. 2003, *ApJ*, **585**, 1147
 Scudder, J. D., & Olbert, S. 1979a, *JGR*, **84**, 2755
 Scudder, J. D., & Olbert, S. 1979b, *JGR*, **84**, 6603
 Shaaban, S. M., Lazar, M., & Poedts, S. 2018, *MNRAS*, **480**, 310
 Shoda, M., Chandran, B. D. G., & Cranmer, S. R. 2021, *ApJ*, **915**, 52
 Squire, J., Chandran, B. D. G., & Meyrand, R. 2020, *ApJL*, **891**, L2
 Štverák, Š., Maksimovic, M., Trávníček, P. M., et al. 2009, *JGR*, **114**, A05104
 Svalgaard, L., & Wilcox, J. M. 1974, *Sci*, **186**, 51
 Tenerani, A., Velli, M., Matteini, L., et al. 2020, *ApJS*, **246**, 32
 Vasko, I. Y., Krasnoselskikh, V., Tong, Y., et al. 2019, *ApJL*, **871**, L29
 Verscharen, D., Chandran, B. D. G., Jeong, S.-Y., et al. 2019, *ApJ*, **886**, 136
 Vocks, C. 2012, *SSRv*, **172**, 303
 Vocks, C., & Mann, G. 2003, *ApJ*, **593**, 1134
 Vocks, C., & Mann, G. 2009, *A&A*, **502**, 325
 Vocks, C., Mann, G., & Rausche, G. 2008, *A&A*, **480**, 527
 Whittlesey, P. L., Larson, D. E., Kasper, J. C., et al. 2020, *ApJS*, **246**, 74
 Woodham, L. D., Horbury, T. S., Matteini, L., et al. 2021, *A&A*, **650**, L1
 Woolley, T., Matteini, L., Horbury, T. S., et al. 2020, *MNRAS*, **498**, 5524
 Yamauchi, Y., Suess, S. T., Steinberg, J. T., et al. 2004, *JGRA*, **109**, A03104
 Zank, G. P., Nakanotani, M., Zhao, L.-L., et al. 2020, *ApJ*, **903**, 1